EXPERIMENTAL INVESTIGATION OF AERODYNAMICAL AND ACOUSTICAL PROPERTIES OF AN UNDEREXPANDED SUPERSONIC JET WITH FORWARD FLIGHT EFFECT

Benoît André[(1)], **Thomas Castelain**[(1)], **Christophe Bailly**[(1)]
[(1)] *Laboratoire de Mécanique des Fluides et d'Acoustique, École Centrale de Lyon,*
36 avenue Guy de Collongues, 69134 Écully CEDEX, France, Email : benoit.andre@ec-lyon.fr

A coaxial supersonic facility has been installed in the anechoic room of the Centre Acoustique (LMFA, Ecole Centrale de Lyon) to reproduce a supersonic fan flow in forward flight. This paper first presents this new facility and some validation tests. To get further insight into the shock-associated noise, Schlieren visualizations as well as near- and far-field acoustic measurements have been performed. Shock cell lengths are shown to be in agreement with the literature, as also the effect of forward flight. A and B screech modes are investigated. It is found that near-field microphones can well discriminate very well between those two, and that mode B has a chaotic behaviour. The effect of secondary flow on screech tones, broadband shock-associated noise and turbulent mixing noise is investigated too. It is shown that forward flight has an effect on both frequencies and amplitudes of supersonic jet noise components. Finally, a shock tracking procedure has been developed to estimate shock oscillation amplitudes and frequency, which is found to be the screech frequency.

1 INTRODUCTION

In modern engines, the exit flow is separated into a hot core flow and a cold fan flow by two nozzles. In the latter, there occurs a pressure mismatch at the exit which entails the generation of a shock cell structure in the jet. The design of the next generation long cruise aircrafts will demand additional efforts on the reduction of shock-associated noise [2, 8]. Weight reduction concerns lead to introduce light composite materials in the fuselage of the next Airbus A350 or Boeing Dreamliner B787 whose sound transmission loss are weaker than in the case of traditional materials. Shock-associated noise is then the stronger contributor for the aft cabin interior noise. It can be divided into a broadband component and a narrow band one.

The work of Harper-Bourne & Fisher [7] is considered as the starting point of research on broadband shock-associated noise (BBSAN). They introduced a phased array of stationary acoustic sources positioned at the end of each shock cell to explain BBSAN emission. Tam has defined it as a product of the interaction between large scale disturbances and the shock cell system [24, 25, 28], which has prompted work on shock cell structure [26]. Aerodynamical as well as acoustical measurements have provided insight into the physics of shock-associated noise [14, 21, 22, 23].

Screech is the narrow band shock noise component. Ever since the pioneering work of Powell [18], it has been explained as a feedback process. The main idea is that some hydrodynamic disturbances originating from the nozzle lip interact with the shock cell pattern as they grow whilst being convected downstream, this interaction producing acoustic waves. The latter propagate then in the upstream direction and excite the shear layer near the nozzle lips, which produces disturbances and closes the feedback loop. Since then, many investigators have contributed to the understanding of the screech generation process and have provided means how to annihilate it [4, 5, 13, 19, 20]. In a unifying effort, it was argued that screech is only a particular case of broadband shock-associated noise [27].

The paper is organized as follows. The coaxial facility and instrumentation are provided in section 2. First aerodynamic results are presented in section 3 and section 4 deals with acoustic behaviour. The shock tracking procedure is reported in section 5 and concluding remarks are finally given in section 6.

2 EXPERIMENTAL APPARATUS

2.1 The dual-stream wind tunnel facility

The jet facility of Centre Acoustique - LMFA UMR CNRS 5509 located at Ecole Centrale de Lyon has recently been used for single high Reynolds number subsonic jet studies [3, 6]. A major upgrade offers now the possibility to study coaxial supersonic jets. A dual-stream wind tunnel with a supersonic or primary duct may be embedded in a subsonic or secondary one

(see Fig. 1). The flow in the first one originates from a Centac C60MX2-SH Ingersoll-Rand compressor using dried air. It can deliver a continuous mass flow rate of 1 kg.s^{-1}. A electrically driven valve downstream of the compressor permits the regulation of the primary flow velocity by controlling the mass flow rate. After that, three electrical resistances, with a 64 kW maximal power, allow to heat the flow.
The flow in the subsonic duct is generated by an electronically controlled Neu LAK 4280A ventilator (2 bars pressure difference) delivering a nominal mass flow rate of 15 kg.s^{-1}.

Downstream of the resistances, the tunnels enter the $10 \times 8 \times 8\,\mathrm{m}^3$ anechoic chamber of the LMFA. The supersonic duct then slips within the subsonic one thank to a flexible pipe. In the exit region of the wind tunnel, the two ducts are therefore coaxial. At the end of them are two contoured convergent axisymmetric nozzles. The primary duct is terminated by a $D_p = 38$ mm diameter aluminium nozzle while the secondary nozzle diameter can be either $D_s = 76.5$ mm or $D_s = 200$ mm, both being made out of resin. The lip thickness of the aluminium nozzle is 0.5 mm.

A calibration procedure permits to link secondary flow velocity to ventilator rotation speed while the stagnation pressure and temperature of the supersonic duct are measured by total pressure and thermocouple probes as soon it enters the anechoic chamber. The maximal exit Mach number for both subsonic nozzles was 0.43 while the fully expanded Mach number M_j ranges up to 1.59, corresponding to a nozzle pressure ratio – NPR – of 4.17, for the supersonic nozzle. The NPR is defined as the ratio between the total pressure and the ambient pressure in the anechoic room.

A Pitot tube connected to a 2000 mm H_2O Furness manometer is used to measure the mean velocity in planes perpendicular to the nozzle exit plane. A unidirectional 55P11 Dantec hot wire is plugged into a CTA Dantec Streamline anemometer so as to measure turbulent velocity profiles. A thermocouple sensor is fixed on the Pitot tube. Manometer, anemometer and thermocouple output are connected to a NI PXI analyser linked to a processor. The three sensors were moved thank to an electrically controlled motor device.

Only subsonic operating points for both ducts are considered. The mean velocity profile along with turbulence intensity are shown in Fig. 2. It is visible that the jet is fully homogeneous in both jet cores. As for turbulence intensity, it is below 1 % within the jet cores and about 16-17 % in both shear layers. Although the operating condition of the primary duct is not representative of what it is meant to become, these measurements ensure that the coaxial wind tunnel does not suffer from a severe trouble.

2.2 Instrumentation

A conventional Z-type Schlieren system was used to visualize the global structure of the choked jet. It consisted of a fibered continuous QTH light source whose adjustable electrical power ranged up to 250 W and of two $\lambda/8$, 107.95 mm diameter, 863.6 mm focal length parabolic mirrors. The off-axis use of the mirrors was limited to $2\,\alpha = 10°$ in order to reduce aberrations. A simple knife edge played the role of the spatial filter. The Schlieren images were recorded by a Phantom V12 CMOS camera, capable of 6 kHz frame rate at full frame size.

Directivity measurements were also led using a quarter-of-inch microphone mounted on a frame rotating about the center of the coaxial nozzles in the exit plane at a distance of 1.7 m. The microphone was a PCB 377B01, a B&K 4135 or a B&K 4939 depending on each individual case, whose measured signal was sampled at 102400 Hz using a NI PXI 5733 board.

Tab. 1 gives an overview of the operating points which are especially considered in this paper and how they are considered.

3 AERODYNAMIC RESULTS

3.1 The shock cell structure

In this section, the shock cell structure obtained by Schlieren visualization is addressed. It was interesting to get a Schlieren picture of the entire jet in order to see the global structure of the shock cell system. Due to the relatively large nozzle exit diameter compared to the Schlieren system mirrors diameter, just one flow visualization was not sufficient because of the small number of shock cells that could then be seen. Translation of the Schlieren system along the jet axis permitted to record images of the flow up to fifteen primary nozzle diameters away from the exit plane. Because of the shock motions, the images had to be averaged to compute a faithful image of the flow. Then, a dedicated algorithm, illustrated further in 5.1, was used to put the pieces together. The result of this procedure is displayed in Fig. 3, where thousand consecutive images were averaged before the montage. It has to be

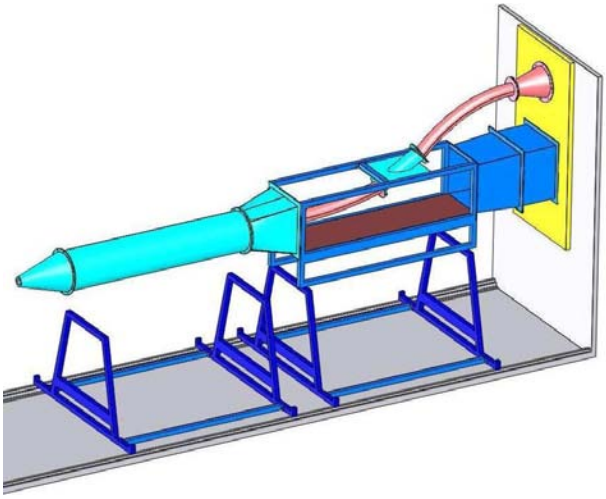

Figure 1: *Sketch of the coaxial facility. Flows run to the left. The supersonic duct is in red, the subsonic one in blue.*

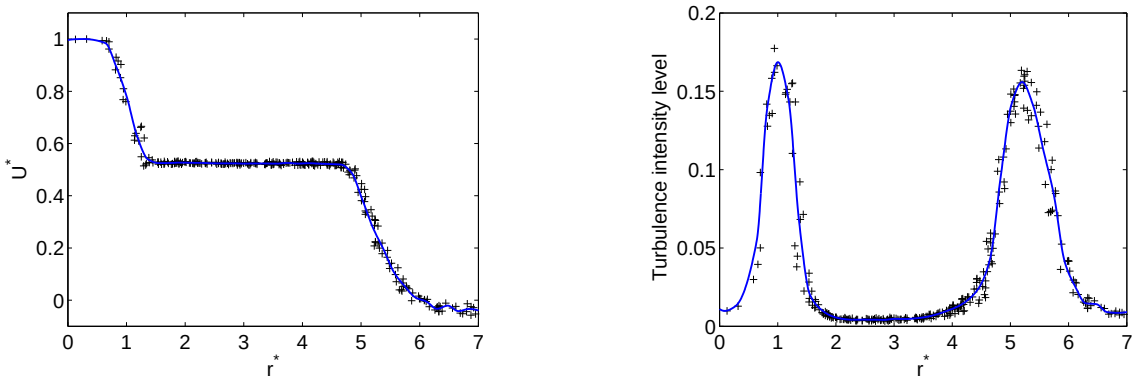

Figure 2: *Left : mean velocity profile against radial position ;* $U^* = U/U_p$ *is the ratio of mean velocity over the primary jet exit velocity (*U_p *= 163 m.s*$^{-1}$*) and* $r^* = r/r_p$ *denotes the radial location divided by the primary nozzle radius. Right : turbulence intensity levels against* r^**, computed by the ratio of RMS fluctuating velocity over the mean velocity difference between the two adjacent flows. The profiles are plotted from 291 measurement points uniformly distributed in a vertical plane 0.5* D_p *downstream of the exit.* D_s *= 200 mm.*

Table 1: *Overview of the primary duct operating points considered in this paper.*

NPR	turbulent mixing noise & BBSAN	screech	secondary flow effect on acoustics	collage	shock tracking
2.27		×			×
2.33				×	
2.54		×			
3.17	×		×		
4.20				×	

noted that the two images of Fig. 3 have same scale, which can be verified in measuring the nozzle diameter visible on the left of both pictures, the flow streaming to the right. The qualitative evolution of the shock cell length with the NPR is then obvious : it increases as the pressure ratio increases. It is also visible that the shock spacing decreases slightly as one moves further downstream [7, 22].

The so-called diamond configuration [1] is displayed in Fig. 3 (bottom). Released from the nozzle, the slightly underexpanded jet overexpands (white right-pointing triangle) but then undergoes a compression (dark left-pointing triangle) which put the jet right back at about the same condition as at the nozzle exit, hence the pseudoperiodic shock cell pattern. Moving downstream, the shear layer spreads which smooths out the pressure oscillation.

The jet structure visible in Fig. 3 (top) matches quite good the sketch of an highly underexpanded jet from [1] as well as the first developments visualized in [17]. The prominent feature of such a jet is the normal shock called Mach disc, formed at the intersection of intercepting shocks (upstream of the disc) and reflected ones (downstream). Behind the edges of the Mach disc, the slipstreams are visible, as slip lines between supersonic flow that did not go through the disc and subsonic flow that did.

3.2 Shock cell length

It is possible from the averaged images to measure the shock spacings and to display their evolution. This was made for various operating conditions and compared to the results of several investigators. The second shock cell length is displayed in Fig. 4. The general agreement with between the various results is to be noted.

Another interesting matter to investigate into is the influence of a secondary flow on the described shock cell structure. With the 76.5 mm secondary nozzle mounted, it was seen that the shock cells lengthen as the secondary flow strengthens but very slightly (less than 3 % increase for a secondary flow Mach number smaller than 0.25). This is qualitatively in accordance with the analytical model of [12]. A duplication of the first shock could also be spotted. The one part of the duplicated shock moves downstream faster than the other part as the dual stream velocity increases. This led to the appearance of a lambda shaped shock.

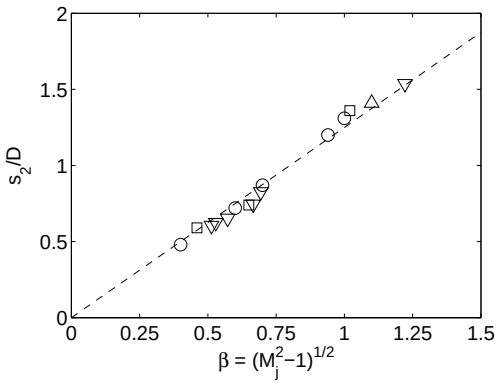

Figure 4: *Comparison of the 2nd shock cell length s_2 of the present study with other investigators. D is the supersonic nozzle exit diameter.* ○ *Norum & Seiner* [14], □ *Panda & Seasholtz* [17], △ *Nouri & Whitelaw* [15], ▽ *present study, −−− linear law of* [7] *and* [22].

4 ACOUSTIC BEHAVIOUR

4.1 Jet screech

Screech tones have been a constant of virtually all measurements and will be dealt with in this section. To ensure that we are dealing with screech and not some other feedback loop, it seemed necessary to investigate into the properties of our narrow band tone and to compare them with well-known screech characteristics in circular jets. The nozzle pressure ratio in the various acoustic measurements ranges from 1.58 to 3.21, all of which is below 1.89 generating a subsonic flow, then uninteresting here.

A decrease in screech frequency and a jump at some point were clearly noticed while continuously increasing the NPR, which is in accordance with the screech behaviour. The frequency jump betrays the modal feature of screech in circular jets, first addressed in Powell's pioneering work [18]. The separation between the first two modes occured approximately at the expected position [19]. The directivity of the narrow band tone was also measured in a horizontal plane centered on the nozzle in 10° steps from $\theta = 30°$ (downstream) to $\theta = 130°$ (upstream), θ being the angle from the nozzle outlet axis to the microphone position. For each position, a narrow band spectrum was recorded, which permitted to compare the strengths of the various harmonics of the tone. It appeared that the fundamental tone was prominent in the upstream and downstream directions and that the first harmonic dominated at $\theta = 90°$. This is consistent with directivity properties of screech tones [13, 18].

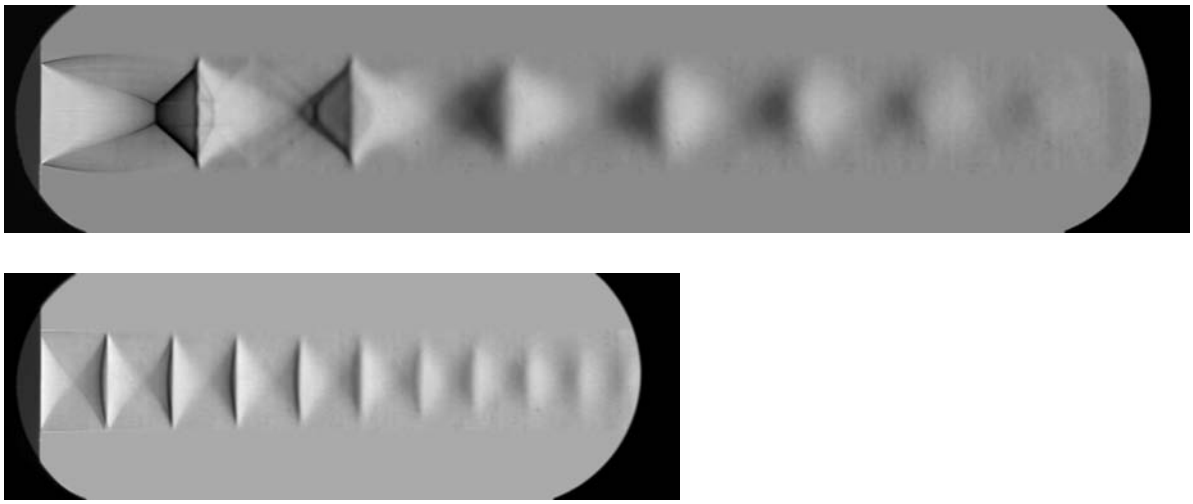

Figure 3: *Collage of several axially translated mean Schlieren pictures of a single stream jet. Top : NPR = 4.20, eight images put together. Bottom : NPR = 2.33, four images put together.*

To be more quantitative in the determination of the nature of the narrow band tone in the measurements, one can compare the measured frequencies of the fundamental tones with the predicted screech frequencies, by means of some analytical formulæ. Two different expressions were considered here. The first one was proposed by Powell [18] :

$$f_s = \frac{1}{3(\mathrm{NPR} - \mathrm{NPR_c})^{1/2}} \frac{a_\infty}{D_p} \quad \text{with} \quad \mathrm{NPR_c} = \left(\frac{\gamma+1}{2}\right)^{\gamma/(\gamma-1)}, \tag{1}$$

where f_s is the screech frequency, $\mathrm{NPR_c}$ the critical nozzle pressure ratio approaching 1.89 for air and a_∞ the speed of sound in ambient medium. The second estimation is given by Raman [20]

$$f_s = \frac{u_c}{s(1 + u_c/a_\infty)}, \tag{2}$$

where u_c is the convection velocity of turbulent structures in the shear layer of the jet, evaluated here at 70 % of the jet fully expanded velocity u_j, and s the shock cell spacing of the imperfectly expanded jet, measured from Schlieren visualizations. It is worth noting that these expressions do not account for the modal behaviour of screech tones. Tab. 2 shows the result of this comparison for some operating conditions that will show up in the following. It is believed that the agreement between measured and computed frequency is acceptable, and it has to be noticed that the measured frequency lays in each case between the two predicted frequencies.

As a conclusion to this narrow band tone characterization, it seems reasonable to assume that the tone arising in the present study be indeed a screech tone and not a spurious reflection or any other artefact.

4.2 Screech modes

As already pointed out in section 4.1, the screech has a modal behaviour. Two modes or stages are discernable in this NPR range. By following Powell [18], the first two modes are referred to as A and B modes. Actually, since Merle [11], the first stage has been divided into two parts, A1 and A2. Only one of them is visible here. The reader can refer to [19] about screech modes.

Two quarter-of-inch microphones have been set just upstream of the nozzle exit in a vertical plane centered on the nozzle, one below the jet and the other above it. Time signals provided by the transducers are shown in Fig. 5 over a short interval. One striking feature showed here is the true sinusoid which denotes a strong screech tone. Also remarkable is the clearly defined relationship between the two measured signals at each NPR. At the lower one, one can observe two in-phase signals which indicate a symmetric screech stage. Mode A is indeed a symmetric one. At the upper NPR, the signals obviously show an opposite phase relation which is consistent with a antisymmetric B mode. The literature distinguishes between several antisymmetrical stages but more microphones would be needed to investigate further in this direction.

One interesting feature is the behaviour of B mode. Displaying the entire measured signal (one second

Table 2: *Comparison between the measured frequency of the fundamental narrow band tones and the predicted screech frequencies.*

NPR	measured frequency (Hz)	screech prediction from [18] (Hz)	error	screech prediction from [20] (Hz)	error
2.27	5669	4869	0.14	6463	0.14
2.54	3939	3719	0.06	4773	0.2

duration), the unsteadiness of the screech level is to be noted. The steadiness of the microphone outputs for the modes A and B are compared in Fig. 6. Few studies [11] pointed out the instability of B mode. Others [9, 19] revealed the unsteadiness of D mode. Further input are needed to explain these instabilities.

Along with screech tones, broadband shock-associated noise (BBSAN) and turbulent mixing noise are also supersonic jet noise components and will be addressed to in the following.

4.3 Effect of the secondary flow on the jet noise

The influence of the secondary stream on jet noise characteristics is now considered. Firstly, directivity properties of BBSAN and turbulent mixing noise are displayed in Fig. 7 where no secondary flow is set. Turbulent mixing noise is especially visible at $\theta = 30°$, while BBSAN consists in the broadband humps peaking at higher frequencies than the fundamental screech tone and is visible for greater angles. The characteristics of these noise components are consistent with their known features [25, 27, 29].

It was observed that the turbulent mixing noise level decreased with secondary flow velocity for a wide range of primary and secondary flow velocities. This tendency is explained by lesser velocity gradients across the inner shear layer, which represents the major contribution to mixing noise emission.

The effect of secondary flow on screech tones and BBSAN is displayed in Fig. 8. The screech amplitude is seen here to increase slightly, which is in general the case. The screech frequency consistently falls when the secondary flow strengthens. This can be explained by a simple argument. If one assumes that a secondary flow has little effect on the inner part of the feedback loop (that is, within the flow – this seems correct as far as the shock cell spacing is concerned, see 3.2), the tone producing process will remain unchanged as a secondary flow arises. The whole effect will then concentrate on the outer part

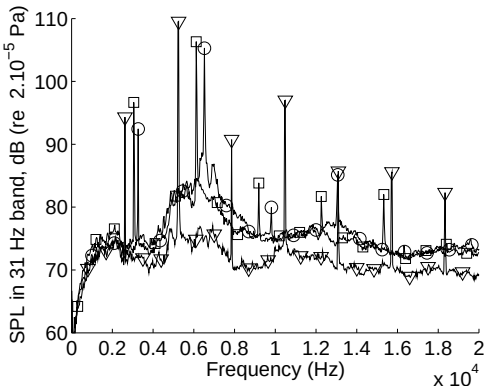

Figure 8: *Effect of the secondary flow Mach number M_s on acoustic spectra , NPR = 3.17, $\theta = 90°$, D_s = 200 mm. ○ M_s = 0, □ M_s = 0.07, ▽ M_s = 0.34.*

of the loop, which is the sound propagation outside the choked flow. A contrary velocity in this part will slow down the upstream propagation acoustic waves and then have a similar effect to that of a decrease in the speed of sound. Looking back at Eq. (1) or Eq. (2), a decrease in the screech frequency is to be expected, which is indeed correlated by the experimental results.

Secondary flow has the same effect on BBSAN frequency as on screech frequency. Moreover, it seems that the sound level decreases more often than not as the secondary flow strengthens, but this is not always the case. This could imply that other effects have to be accounted for.

The last section is devoted to develop a shock tracking procedure to characterize screech-induced shock oscillations.

5 SHOCK OSCILLATIONS

5.1 Shock tracking procedure

Shocks in a screeching jet oscillate at the screech frequency [16]. In order to see that, a sampling frequency greater than twice the screech one is needed. In the NPR = 2.27 case from Fig. 5 (left), the screech

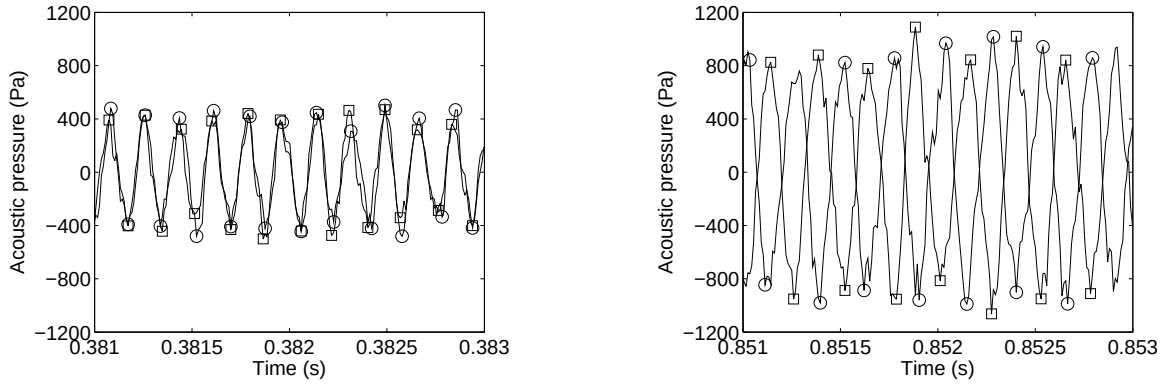

Figure 5: *Time signals from two microphones located on either side of the nozzle (denoted by ○ and □). Left, NPR = 2.27 and right, NPR = 2.54.*

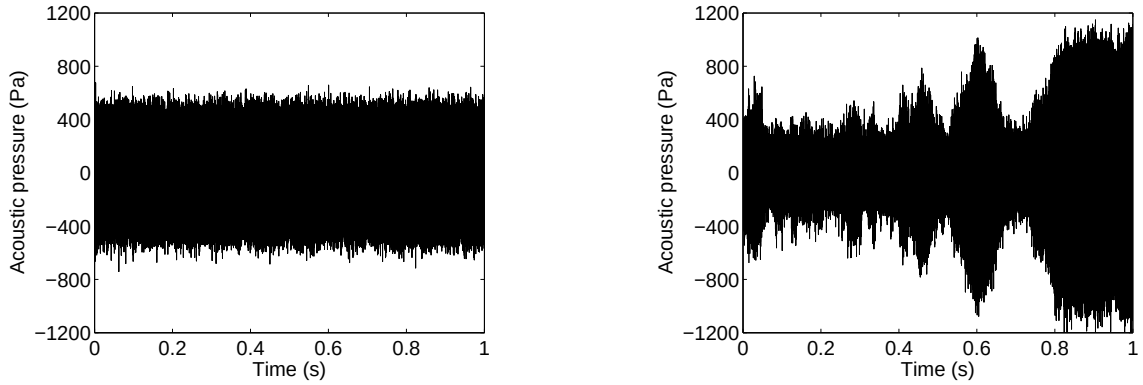

Figure 6: *Time signals over one second recorded from one microphone located on the nozzle. Left, NPR = 2.27 and right, NPR = 2.54.*

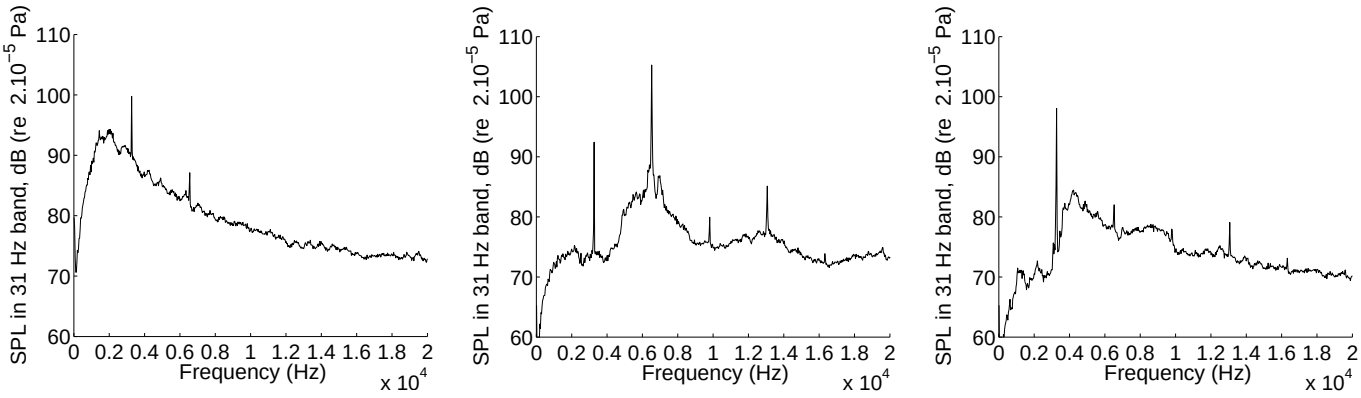

Figure 7: *Directivity of the turbulent mixing noise and the BBSAN. NPR = 3.17. Left, $\theta = 30^\circ$, middle, $\theta = 90^\circ$ and right, $\theta = 130^\circ$.*

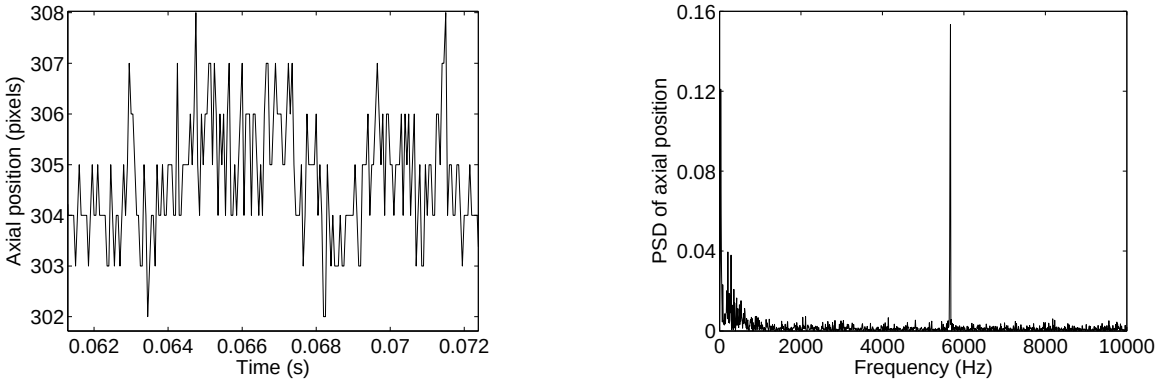

Figure 9: *Left : axial oscillation of the tip of the first shock for NPR = 2.27 ; right : power spectral density of the axial position signal, spectral resolution of 10 Hz. Parameters of tracking procedure are :* $N = M = 10, n = m = 30$.

frequency was 5669 Hz. Synchronized Schlieren acquisition was made at a sampling frequency of 20 kHz which was then enough to track the motion of the shock. No secondary flow is considered in this section.

A pattern matching algorithm developed by Kegerise & Settles [10] was adapted. The idea is to isolate a reference image and then track the motion of a reference patch within the reference image in the subsequent ones. This is done by finding the minimal error in a correlation map. Errors are defined as :

$$E(i_0, j_0, \Delta i, \Delta j) = \sum_{\delta i} \sum_{\delta j} [g_1(i_0 + \delta i, j_0 + \delta j) - g_2(i_0 + \delta i + \Delta i, j_0 + \delta j + \Delta j)]^2 \quad (3)$$

In Eq. (3), E is the error estimation between the reference image of grayscale pixel 2D function g_1 and any of the subsequent images of grayscale map g_2. (i_0, j_0) are the coordinates of the selected reference point, centered on a distinctive shock pattern whose motion one seeks to determine. The reference patch is a $(2n + 1) \times (2m + 1)$ pixel large window centered on (i_0, j_0). It is defined by the summation interval over $(\delta i,\ \delta j) \in [|-n; n|] \times [|-m; m|]$. One computes the error between this reference patch and any patch of same size moving in a window of candidates for the new position of (i_0, j_0), according to $\Delta i \in [|-N; N|]$ and $\Delta j \in [|-M; M|]$. This procedure delivers a map on which the better match between the two pictures is found by searching the minimal error. Looping over a whole range of consecutive Schlieren images makes it possible to track down the radial and axial motions of shocks.

Without any further treatment, noisy results were achieved. Indeed, turbulent fluctuations of density imply fluctuations of refraction index and hence of grayscale level on the Schlieren pictures. Considering two different images, turbulent fluctuations at one position are uncorrelated. As a consequence, turbulence will interfere in the pattern matching algorithm and bring the procedure to fail occasionally, hence the noise. But shocks are well defined in the Schlieren visualizations (see 3.1) and can be at the first sight isolated because of their low grayscale levels. This simple statement can be built on to purified the computed shock motion if one transforms all the images prior to applying the algorithm in the following way : one clips the bright enough pixels and stretches the remaining intensity levels from 0 to the maximum level (255 for 8-bit pictures). The cutoff grayscale level is chosen so as to discriminate between the darker shocks and their brighter surroundings. So, all turbulent fluctuations visible outside the shocks are crushed and the results of the matching algorithm are much cleaner.

The axial oscillation of the tip of the first shock for the quoted case of NPR = 2.27 or M_j = 1.15 is given in Fig. 9 over a 2048 images interval corresponding to just above 0.1 s. One can get from this plot that the amplitude of oscillation of the first shock cell is of about 4-5 pixels or 0.5 mm, which is close to the 0.6 mm Panda [16] found at M_j = 1.19. It is visible in Fig. 9 that the dynamic range and the frame rate of the displayed signal are limited. This will be corrected in subsequent studies. It also has to be said that this tracking procedure is practically limited to the first shock in most cases because one needs well defined shocks and pronounced intensity contrast to the surroundings to get clean results.

5.2 Application to the determination of oscillation frequencies

From the successive axial position signal, one can compute the power spectral density of the oscillating movement, as displayed in Fig. 9 (right). The striking feature of this spectrum is the dominant narrow band peak visible at 5670 Hz ($\pm$ 5 Hz), which corresponds almost exactly to the measured acoustic screech frequency of 5669 Hz ($\pm$ 0.5 Hz). This result confirms that the screech makes the whole jet oscillate at its frequency, which is in agreement with the work of Panda [16].

6 CONCLUDING REMARKS

This paper presented the first results obtained in the upgraded jet facility of the Centre Acoustique (LMFA & Ecole Centrale de Lyon). A Schlieren system has been mounted to gain some insight into the structure of an underexpanded supersonic jet and to compare it to some known features. While setting a secondary flow, a lengthening of the shock spacings was observed as well as a duplication of the first shock and the formation of a lambda shape. Acoustical measurements were also made in an anechoic environment. The so-called A mode and B mode of screech were investigated. It is shown that the signals from two opposite microphones are well in-phase and in opposite phase relation for A and B modes respectively. Mode B displays some chaotic variations. The general acoustic properties of the three supersonic jet noise components were displayed. The influence of a secondary flow seems to read as follows : a diminution of the turbulent mixing noise, a decrease in screech frequency along with a slight increase in its amplitude and a decrease in broadband shock-associated noise peak frequency coming with a decrease in its amplitude. Finally, a shock tracking algorithm has been developed and results confirm that a screeching jet oscillates at the screech frequency.

This work is currently in progress. Pressure probe surveys are to be made along with laser Doppler velocimetry (LDV) in order to better understand the physics of the shock cells and to link it with the Schlieren visualizations. Phase averaging of the latter should allow to obtain another point of view on jet oscillation. LDV measurements should also allow to investigate into the evolution of turbulence across shocks. Finally, a sensitivity enhanced Schlieren system will be mounted, especially to further work on the growth of instability waves in the shear layer between primary and secondary flow.

References

[1] Adamson, T. C., and Nicholls, J. A. On the structure of jets from highly underexpanded nozzles into still air. Tech. Rep. ERI Project 2397, The University of Michigan, Detroit, 1958.

[2] Calkins, F. T., Butler, G. W., and Mabe, J. H. Variable geometry chevrons for jet noise reduction. *AIAA Paper*, 2006-2546 (2006).

[3] Castelain, T., Sunyach, A., Juve, D., and Bera, J.-C. Jet-noise reduction by impinging microjets: An acoustic investigation testing microjet parameters. *AIAA Journal 46*, 5 (2008), 1081–1087.

[4] Davies, M. G., and Oldfield, D. E. S. Tones from a choked axisymmetric jet. I. cell structure, eddy velocity and source locations. *Acustica 12*, 4 (1962), 257–266.

[5] Davies, M. G., and Oldfield, D. E. S. Tones from a choked axisymmetric jet. II. the self excited loop and mode of oscillation. *Acustica 12*, 4 (1962), 267–277.

[6] Fleury, V., Bailly, C., Jondeau, E., Michard, M., and Juve, D. Space-Time correlations in two subsonic jets using dual particle image velocimetry measurements. *AIAA Journal 46*, 10 (2008), 2498–2509.

[7] Harper-Bourne, M., and Fisher, M. J. The noise from shock waves in supersonic jets. *AGARD Conference on Noise Mechanisms*, 1311973 (1973).

[8] Huber, J., Sylla, A. A., Fleury, V., Bulté, J., Britchford, K., Laurendeau, E., and Long, D. Understanding and reduction of cruise jet noise at model and full scale. *AIAA Paper*, 2009-3382 (2009).

[9] Jothi, T. J. S., and Srinivasan, K. Role of initial conditions on noise from underexpanded pipe jets. *Physics of Fluids 21*, 6 (2009).

[10] Kegerise, M. A., and Settles, G. S. Schlieren image-correlation velocimetry and its application to free-convection flows. *9th International Symposium on Flow Visualization*, 380 (2000).

[11] Merle, M. Sur la fréquence des ondes émises par un jet d'air à grande vitesse. C. R. 243, Académie des sciences de Paris, 1956.

[12] Morris, P. J. A note on the effect of forward flight on shock spacing in circular jets. *Journal of Sound and Vibration 122*, 1 (1988), 175–177.

[13] Norum, T. D. Screech suppression in supersonic jets. *AIAA Journal 21*, 2 (1983), 235–240.

[14] NORUM, T. D., AND SEINER, J. M. Measurements of mean static pressure and far field acoustics of shock containing supersonic jets. NASA Technical Memorandum 84521, NASA, 1982.

[15] NOURI, J. M., AND WHITELAW, J. H. Flow characteristics of an underexpanded jet and its application to the study of droplet breakup. *Experiments in Fluids 21*, 4 (1996), 243–247.

[16] PANDA, J. Shock oscillation in underexpanded screeching jets. *Journal of Fluid Mechanics 363* (1998), 173–198.

[17] PANDA, J., AND SEASHOLTZ, R. G. Measurement of shock structure and shock-vortex interaction in underexpanded jets using rayleigh scattering. *Physics of Fluids 11*, 12 (1999), 3761–3777.

[18] POWELL, A. On the mechanism of choked jet noise. *Proceedings of the Physical Society of London 66*, 408 (1953), 1039–1056.

[19] POWELL, A., UMEDA, Y., AND ISHII, R. Observations of the oscillation modes of choked circular jets. *Journal of the Acoustical Society of America 92*, 5 (1992), 2823–2836.

[20] RAMAN, G. Supersonic jet screech: Half-century from powell to the present. *Journal of Sound and Vibration 225*, 3 (1999), 543–571.

[21] RAMAN, G., AND RICE, E. J. Instability modes excited by natural screech tones in a supersonic rectangular jet. *Physics of Fluids 6*, 12 (1994), 3999–4008.

[22] SEINER, J. M., AND NORUM, T. D. Aerodynamic aspects of shock containing jet plumes. *AIAA Paper*, 80-0965 (1980).

[23] SEINER, J. M., AND YU, J. C. Acoustic near-field properties associated with broadband shock noise. *AIAA Journal 22*, 9 (1984), 1207–1215.

[24] TAM, C. K. W. Supersonic jet noise generated by large scale disturbances. *Journal of Sound and Vibration 38*, 1 (1975), 51–79.

[25] TAM, C. K. W. Supersonic jet noise. *Annual Review of Fluid Mechanics 27* (1995), 17–43.

[26] TAM, C. K. W., JACKSON, J. A., AND SEINER, J. M. A Multiple-Scales model of the Shock-Cell structure of imperfectly expanded supersonic jets. *Journal of Fluid Mechanics 153* (1985), 123–149.

[27] TAM, C. K. W., SEINER, J. M., AND YU, J. C. Proposed relationship between broadband shock associated noise and screech tones. *Journal of Sound and Vibration 110*, 2 (1986), 309–321.

[28] TAM, C. K. W., AND TANNA, H. K. Shock associated noise of supersonic jets from convergent-divergent nozzles. *Journal of Sound and Vibration 81*, 3 (1982), 337–358.

[29] ZAMAN, K. B. M. Q., AND YU, J. C. Power spectral density of subsonic jet noise. *Journal of Sound and Vibration 98*, 4 (1985), 519–537.